


Secondary Bubble Entrainment via Primary Bubble Bursting at a Viscoelastic Surface

Bingqiang Ji^{1,*}, Zhengyu Yang¹, Zirui Wang¹, Randy H. Ewoldt^{1,2,3} and Jie Feng^{1,3,†}

¹*Mechanical Science and Engineering, University of Illinois at Urbana-Champaign, Urbana, Illinois 61801, USA*

²*Beckman Institute for Advanced Science and Technology, University of Illinois at Urbana-Champaign, Urbana, Illinois 61801, USA*

³*Materials Research Laboratory, University of Illinois at Urbana-Champaign, Urbana, Illinois 61801, USA*

 (Received 25 November 2022; revised 12 June 2023; accepted 24 July 2023; published 7 September 2023)

Bubble bursting at liquid surfaces is ubiquitous and plays a key role for the mass transfer across interfaces, impacting global climate and human health. Here, we document an unexpected phenomenon that when a bubble bursts at a viscoelastic surface of a bovine serum albumin solution, a secondary (daughter) bubble is entrapped with no subsequent jet drop ejection, contrary to the counterpart experimentally observed at a Newtonian surface. We show that the strong surface dilatational elastic stress from the viscoelastic surface retards the cavity collapse and efficiently damps out the precursor waves, thus facilitating the dominant wave focusing above the cavity nadir. The onset of daughter bubble entrainment is well predicted by an interfacial elastocapillary number comparing the effects of surface dilatational elasticity and surface tension. Our Letter highlights the important role of surface rheology on free surface flows and may find important implications in bubble dynamics with a contaminated interface exhibiting complex surface rheology.

DOI: [10.1103/PhysRevLett.131.104002](https://doi.org/10.1103/PhysRevLett.131.104002)

Bubbles are widely present at liquid surfaces and mediate the mass and momentum transport across interfaces in many natural and industrial processes [1,2]. For instance, bursting bubbles produce film and jet drops as the main source of sea spray aerosols [3–5], impacting atmospheric radiation and global climate [6–8]. These drops can be enriched with microplastics and pathogens from the bulk liquids [9,10], threatening human health [11,12]. Additionally, bubble bursting flows can induce intense strain rates causing cell damage in bioreactors and vegetative reproduction in the ocean [13,14]. Thus, the dynamics of bubble bursting has received extensive attention over the past decades.

A structurally complex liquid surface usually exists due to the contaminants or the biological processes in liquids [15,16] and may significantly modify the dynamics of bubble bursting. For example, an oil-covered aqueous interface introduces extra viscous dampings to the bubble cavity collapse, dramatically changing the jet radius and velocity [17,18]. Additionally, surfactants can inhibit the jetting by introducing the Marangoni effect that retards the cavity collapse and jet growth [19–21]. In fact, the structurally complex surface may also exhibit intrinsic surface rheology such as viscoelasticity caused by macromolecule interactions, exemplified by the surface microlayer containing gel-like proteins or microorganisms in natural water bodies or bioreactors [16,22]. Though the surface viscoelasticity has been found to profoundly modify the bubble cap film rupture dynamics recently [23], its role in the subsequent cavity collapse and jet formation remains elusive.

Here, we report an unexpected phenomenon that the surface viscoelasticity triggers secondary (daughter) bubble

entrainment and suppresses the subsequent jetting during bubble bursting. More importantly, we rationalize the essential role of the surface dilatational elasticity behind this phenomenon by considering an interfacial elastocapillary number. These findings demonstrate that surface rheology can remarkably affect free surface flows and reshape the dynamics of mass transfer relevant to bubble bursting.

To signify the role of surface viscoelasticity in a controllable way, we use bovine serum albumin (BSA), a widely studied model protein, dissolved in a NaCl buffer to form a viscoelastic surface while the bulk liquid exhibits Newtonian behavior [24]. The globular BSA molecules irreversibly adsorb to the liquid-gas interface without denaturation [25], forming an interconnected network within the adsorbed layer with high storage modulus upon compression [26,27]. The addition of surfactants can drastically change the surface properties of the BSA solution, giving a variety of model systems with desired surface properties by tuning the surfactant concentration [23,28]. A bubble of radius $R \approx 1.1$ mm is released to the liquid surface (see Supplemental Material [29] Secs. S1–S4 for experimental details), where the static bubble shape is not affected by the adsorbed protein layer. After the bubble cap rupture (defined as $t = 0$), the bubble cavity collapses with a series of capillary waves propagating downward. At a low BSA concentration (C_{BSA}), referred to as the jetting regime [Fig. 1(b)], the focusing of capillary waves at the cavity nadir ejects an upward jet, which finally breaks up and produces jet drops, similar to bubble bursting at a clean surface [Fig. 1(a)]. On the contrary, at a large C_{BSA} , referred to as the entrainment regime [Fig. 1(c)], a highly deformed,

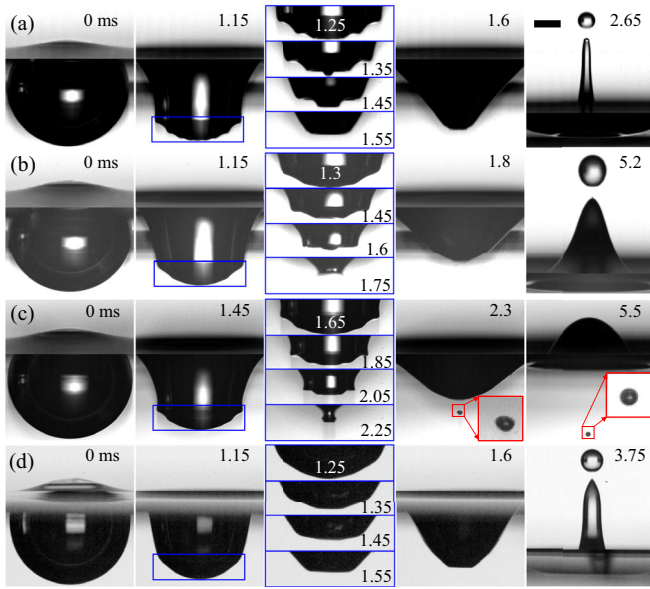


FIG. 1. High-speed observations of bubble bursting dynamics at (a) a clean aqueous surface, BSA solution surfaces with C_{BSA} of (b) 0.01 g/L and (c) 0.05 g/L, and (d) a surface of a 0.01 g/L ($0.64 \times \text{CMC}$) Tween 80 solution. $t = 0$ represents the beginning of bubble bursting. Here, the bubble radius $R = 1.1 \pm 0.1$ mm and aging time $t_a = 20$ s. Videos are provided in Supplemental Material [29]. Scale bar is 0.5 mm.

small daughter bubble is entrapped at the cavity nadir and no jet drop ejection is observed.

Similar to surfactants, BSA could lower the surface tension and induce Marangoni stresses at the surface [36]. However, when a bubble bursts at a small-molecule surfactant Polysorbate 80 (Tween 80) solution surface with $0.1\text{--}10 \times$ critical micelle concentration (CMC), no bubble entrainment is observed [Fig. 1(d)], consistent with previous experimental observations using sodium dodecyl sulfate (SDS) [20]. Moreover, jet drop ejection is found to be only suppressed near CMC in an SDS solution [20], while jet drop ejection is killed over a wide BSA concentration range in our study. Therefore, we believe that the bubble

entrainment and jetting suppression are triggered by the intrinsic viscoelasticity properties of the adsorbed BSA layer.

To determine the transition between the jetting and entrainment regimes, we experimentally explore the parameter space spanned by C_{BSA} and the bubble aging time t_a (the time from bubble generation to bursting), considering the continuously evolving surface properties over a long time (\sim hours) due to the slow adsorption kinetics of BSA [27,37]. As shown in Fig. 2(a), with an increasing C_{BSA} , the bubble bursting regime changes from jetting to entrainment, between which a short transition regime exists without jet drops or entrapped bubbles. The lower limit of C_{BSA} for bubble entrainment is 0.01 g/L at $t_a = 300$ and 1200 s and increases to 0.05 g/L at $t_a = 20$ s. The bubble entrainment occurs at a C_{BSA} up to 100 g/L, spanning 4 orders of magnitude. More generally, we also experimentally observed such a daughter bubble entrainment in bubble bursting at the surfaces of lysozyme solutions and micro-particle suspensions (Supplemental Material [29] Sec. S5), indicating the robustness of this intriguing phenomenon.

The dynamics of bubble bursting at a clean surface is determined by the dimensionless numbers $Oh = \mu / (\rho \gamma R)^{0.5}$ (comparing visco-capillary to inertio-capillary timescales) and $Bo = \rho g R^2 / \gamma$ (comparing gravity to capillarity) [38,39], where γ , ρ , μ are the surface tension, density, and viscosity of the liquid, respectively. In our experiments, the gravity effect is minor because $Bo < 0.25$, and the entrainment regime is not expected considering $Oh = 0.003\text{--}0.004$ [40]. However, at a BSA-adsorbed surface, the top jet drop velocity v_d decreases dramatically with increasing C_{BSA} and t_a , indicating a significantly weakened jetting, until the jet drop ejection is completely suppressed [Fig. 2(b)]. Meanwhile, the top jet drop radius r_d does not change drastically in comparison. In the entrainment regime, the daughter bubble radius r_{eb} increases first and then reaches a plateau with increasing C_{BSA} [Fig. 2(c)]. All these findings suggest distinct features and enriched dynamics of bubble bursting introduced by the adsorbed BSA layer.

To further rationalize the role of the adsorbed BSA layer, we first evaluate the BSA kinetics during bubble bursting.

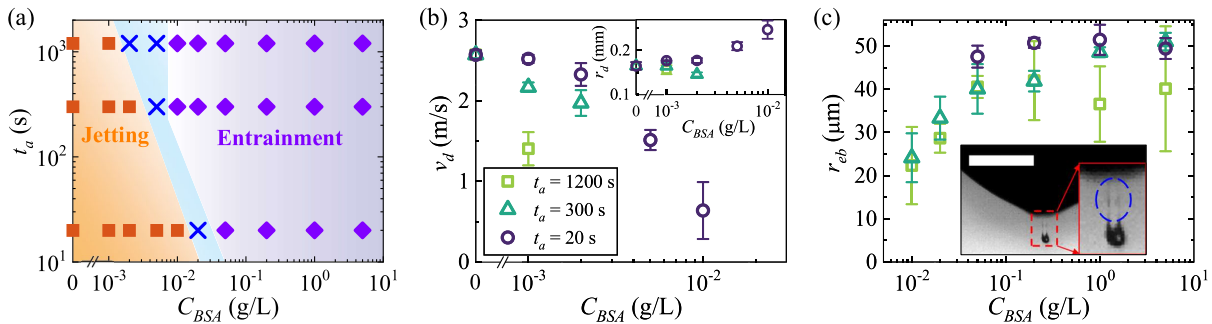


FIG. 2. (a) Regime map of bubble bursting regarding C_{BSA} and t_a , showing three regimes of jetting, transition, and entrainment. $C_{BSA} = 0$ represents a clean NaCl buffer solution without BSA. (b) Velocity v_d and radius r_d (inset) of the top jet drop upon detachment and (c) the daughter bubble radius r_{eb} as functions of C_{BSA} . Inset in (c) shows the shed BSA fragments (highlighted in blue circle) upon daughter bubble pinch-off at $C_{BSA} = 0.2$ g/L and $t_a = 1200$ s. Scale bar is 0.5 mm.

The diffusion of BSA is slow enough to be neglected, considering the large bulk and surface Péclet numbers, calculated as $Pe_b = v_c R / D_b \sim O(10^7)$ (comparing convection to bulk diffusion) and $Pe_s = v_c R / D_s \geq O(10^4)$ (comparing convection to surface diffusion). Here, D_b and D_s are, respectively, the bulk and surface diffusivities of BSA [41,42], $v_c = [\gamma_0 / (\rho R)]^{1/2}$ is the inertio-capillary velocity characterizing the protein convection during cavity collapse, where γ_0 is the surface tension upon bubble bursting (at $t = 0$). Furthermore, the adsorption and desorption of BSA are also negligible during bubble bursting, since $k_a C_{\text{BSA}} R / v_c \leq O(10^{-3})$ (comparing adsorption to convection), and the Biot number $\text{Bi} = k_d R / v_c \sim O(10^{-6})$ (comparing desorption to convection), where k_a and k_d are the adsorption and desorption coefficients [43], respectively. Therefore, the adsorbed BSA layer at the bubble surface acts as an insoluble viscoelastic layer, where the globular BSA molecules are initially uniformly distributed [Fig. 3(a)] and then undergo a redistribution dominated by surface convection upon bursting.

Since both the bubble entrainment and jetting result from the cavity collapse, we then investigate the effect of the adsorbed BSA layer on cavity collapse dynamics. Considering the capillary waves propagating downward, the last and the most energetic one is known as the dominant wave, while the smaller ones in front are the precursor waves. The dominant wave assists the compression of the cavity surface in front forming a high BSA concentration (Γ) region, and it expands the cavity surface behind, forming a low Γ region [Fig. 3(b)]. This sweep effect of propagating waves is also reported numerically in

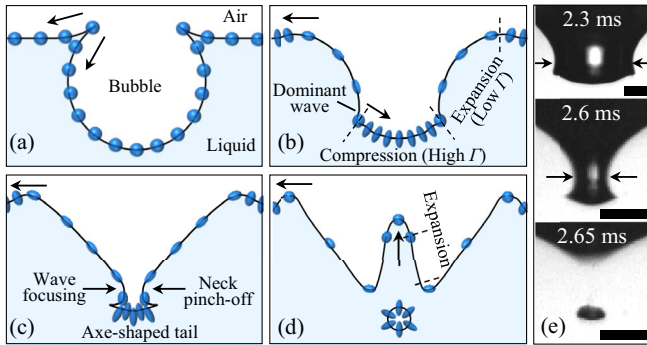


FIG. 3. (a)–(d) Schematics of the surface BSA transport at entrainment regime: (a) BSA molecules (spheres) are distributed uniformly at the cavity surface initially. (b) During cavity collapse, the dominant wave sweeps the BSA molecules toward the bubble bottom. (c) Then an axe-shaped cavity tail enriched with BSA molecules forms, and the neck pinch-off caused by dominant wave focusing entraps a daughter bubble. (d) An upward thick jet arises finally without drop ejection. The dashed lines mark the surfaces experiencing expansion or compression. The arrows represent the flow directions. (e) Experimental images showing wave focusing, neck pinch-off, and bubble entrainment. $C_{\text{BSA}} = 100$ g/L, $t_a = 20$ s. Scale bar is 0.2 mm.

surfactant-laden bubble bursting, where Γ can differ by $O(1-10^2)$ folds along the cavity surface [21]. As a result, the redistribution of BSA at the cavity surface introduces two surface effects, i.e., the Marangoni stress from the surface tension gradient and an extra stress from the surface viscoelasticity of the adsorbed BSA layer [44].

Next, we investigate these above two surface effects during cavity collapse, by considering the resulted surface traction f_e , which acts tangentially at the liquid-gas interface influencing the bubble bursting flows,

$$f_e = (\nabla^s \cdot \boldsymbol{\tau}^s) \cdot \mathbf{t}, \quad (1)$$

where \mathbf{t} is the unit tangential vector, $\nabla^s = \mathbf{I}^s \cdot \nabla$ is the surface gradient operator, and \mathbf{I}^s is the surface identity tensor. $\boldsymbol{\tau}^s$ is the local surface stress expressed as

$$\boldsymbol{\tau}^s = \gamma \mathbf{I}^s + \boldsymbol{\tau}_e. \quad (2)$$

γ is the local surface tension based on the revised Langmuir relation [43,45], written as

$$\gamma = \begin{cases} \gamma_f + R_g T \Gamma_p \ln\left(1 - \frac{\Gamma}{\Gamma_{\max}}\right), & \Gamma < \Gamma_c, \\ \gamma_{\min}, & \Gamma \geq \Gamma_c, \end{cases} \quad (3)$$

where γ_f , γ_{\min} , R_g , T , and Γ_{\max} are the surface tension of a clean surface, minimum surface tension, gas constant, temperature, and saturated BSA surface concentration, respectively. Γ_p is a fitting parameter and $\Gamma_c = \Gamma_{\max} - \Gamma_{\max} \exp[(\gamma_{\min} - \gamma_f) / (R_g T \Gamma_p)]$ (see Supplemental Material [29] Sec. S6 for parameter values). $\boldsymbol{\tau}_e$ is the extra surface stress from surface viscoelasticity. Since the bubble bursting time [$\sim O(1)$ ms] is much smaller than the surface stress relaxation time [$\sim O(1)$ s] for BSA [46], the BSA-adsorbed surface responds as a solidlike elastic surface [43]. Using a linear elastic model for simplicity [47], we have $\boldsymbol{\tau}_e = E_d (\nabla^s \cdot \mathbf{u}) \mathbf{I}^s + E_s [2\mathbf{U}^s - (\nabla^s \cdot \mathbf{u}) \mathbf{I}^s]$, where $\mathbf{U}^s = 1/2[\nabla^s \mathbf{u} \cdot \mathbf{I}^s + \mathbf{I}^s \cdot (\nabla^s \mathbf{u})^T]$ is the interfacial strain tensor, \mathbf{u} is the surface displacement vector, and E_d and E_s are the intrinsic surface dilatation and shear moduli, respectively. Previous studies report that E_s is significantly smaller than E_d for BSA systems [37,48]. In addition, our experiment shows that the cavity evolves to a truncated cone with a nearly flattened base, which is anticipated to experience a deformation of compression with negligible shear, when the angular position of the dominant wave $\theta \lesssim \pi/4$. At the limit of small θ , surface dilatational elasticity dominates compared to shear elasticity (Supplemental Material [29] Sec. S7). At the instant of surface deformation, E_d is characterized by the initial dilatation modulus E_{d0} [23,26]. Considering $\nabla^s \cdot \mathbf{u} = -\ln(\Gamma/\Gamma_0)$ for an insoluble surface layer with Γ_0 as the initial BSA surface concentration (Supplemental Material [29] Sec. S8), we have

$$\tau_e = -E_d \ln\left(\frac{\Gamma}{\Gamma_0}\right) \mathbf{I}^s. \quad (4)$$

Substituting Eqs. (2)–(4) into Eq. (1), we obtain

$$\frac{f_e}{\gamma_0} = -\beta \frac{H(\Gamma_c - \Gamma)}{\Gamma_{\max} - \Gamma} \nabla^s \Gamma \cdot \mathbf{t} - E_c \frac{1}{\Gamma} \nabla^s \Gamma \cdot \mathbf{t}, \quad (5)$$

where the first and second terms on the right-hand side are the Marangoni and dilatational elasticity stresses, respectively, both opposite to the BSA surface concentration gradient $\nabla^s \Gamma$. $\beta = R_g T \Gamma_p / \gamma_0$ is the Marangoni elasticity number comparing the Marangoni effect with the surface tension effect, and $E_c = E_{d0} / \gamma_0$ is the interfacial elastocapillary number comparing surface dilatational elasticity with surface tension. H is the Heaviside function, which equals 1 when $\Gamma < \Gamma_c$ and 0 otherwise. We measure γ_0 and E_{d0} [Fig. 4(a)] using a custom-built bubble tensiometer [49] (Supplemental Material [29] Sec. S3) and obtain that β is < 0.14 , while E_c is up to 1.77 for the BSA systems. Based on the above estimation, for current experiments, Eq. (5) reduces to $f_e / \gamma_0 = -E_c (\nabla^s \Gamma / \Gamma) \cdot \mathbf{t}$.

During cavity collapse, the downward propagating capillary waves generate a downward $\nabla^s \Gamma$, thus yielding an overall upward f_e . This traction retards the cavity collapse by decreasing the velocity of the dominant wave trough v_w , as shown in Fig. 4(b). For bubble bursting at a clean surface, $v_w \approx 5.7 v_c$, consistent with previous work [50]. With increasing C_{BSA} , v_w / v_c sharply decreases at the transition regime and then slowly decreases to < 3 at the entrainment regime. This retardation effect facilitates the appearance of a sharp cusp at the dominant wave trough and a neck at the dominant wave crest at the late stage of cavity collapse [Fig. 3(e)]. Meanwhile, the precursor wave experiences a much higher Γ (or surface viscoelasticity) due to the sweeping effect [Fig. 3(b)]. It is well established that surface viscoelasticity resists the surface deformation that accompanies the wave motion, thus enhancing the capillary wave damping [51]. Consistently, we observe an

increasing damping of precursor waves with increasing C_{BSA} (Supplemental Material [29] Sec. S9). At a small C_{BSA} , the precursor waves cannot be completely damped out and are strong enough to reverse the bubble nadir before dominant wave focusing [Fig. 1(b)], thus no bubble is entrapped. While at a large C_{BSA} , the large surface viscoelasticity completely damps out the precursor waves, preserving a smooth bubble bottom, finally forming an axe-shaped cavity tail [$t = 2.25$ ms in Fig. 1(c)]. This cavity bottom may become more rigid due to the enrichment of BSA under large surface compression, as evidenced by the shed BSA fragments upon pinch-off [Fig. 2(c)], similar to the protein particle shedding from a compressed protein-adsorbed bubble surface reported previously [26]. Thus, the dominant wave can only focus above the rigid axe-shaped cavity tail, triggering the neck pinch-off and entrapping a daughter bubble highly enriched with BSA on the bubble surface [Figs. 3(c) and 3(e)].

Our theoretical analysis suggests that the jetting and entrainment regimes are determined by E_c . Essentially, the surface tension drives the capillary wave propagation that distorts the original smooth cavity surface (associated with a surface energy of density γ_0), while the surface dilatational elasticity resists surface deformation (associated with an elastic energy of density E_{d0}) caused by capillary waves. When $E_c > 1$, the dilatational elasticity outweighs the surface tension and is strong enough to smooth off the precursor waves to form an axe-shaped bubble nadir, triggering the daughter bubble entrainment. Consistently, our experiment shows that $E_c \approx 1$ well captures the onset of the entrainment regime for various t_a and C_{BSA} [Fig. 4(c)]. After cavity collapse, the upward moving jet tip stretches the jet surface and results in an upward $\nabla^s \Gamma$ [19] [Fig. 3(d)], generating a downward traction that retards the growth and breakup of the jet. This finally kills the drop ejection with the increasing E_c at a higher C_{BSA} .

The essential role of surface viscoelasticity is further validated by adding Tween 80, which competes for surface

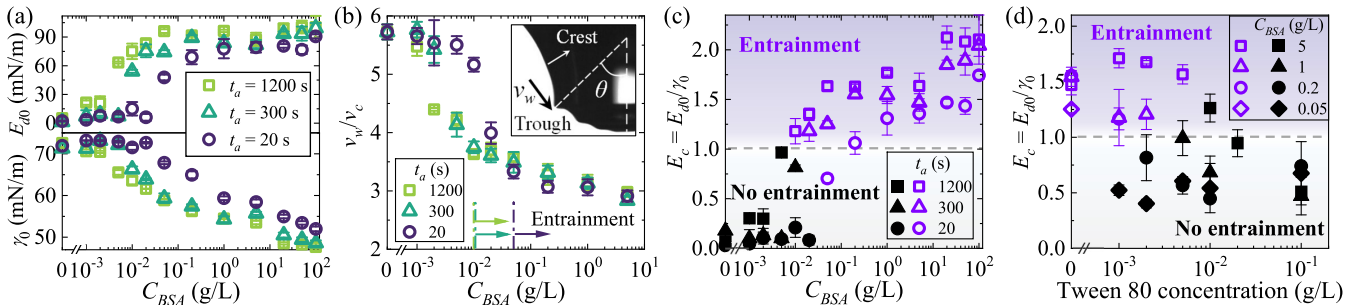


FIG. 4. (a) Initial surface tension γ_0 and initial surface dilatational modulus E_{d0} of BSA solutions and (b) normalized velocity v_w / v_c of the dominant wave trough (at $\theta = \pi/4$, see inset) during bubble cavity collapse as functions of C_{BSA} . Interfacial elastocapillary number E_c of BSA solutions as a function of (c) C_{BSA} at different t_a without addition of Tween 80 and (d) Tween 80 concentration at different C_{BSA} and $t_a = 300$ s with addition of Tween 80, showing the bubble entrainment (open) occurs when $E_c \gtrsim 1$. Adding Tween 80 reduces the surface elasticity and thus suppresses the bubble entrainment.

coverage with BSA. The addition of Tween 80 in BSA solutions reduces the surface elasticity, thus eliminating the bubble entrainment and recovering the jet drop ejection for a wide range of BSA concentrations [Fig. 4(d) and Supplemental Material [29] Sec. S10]. In addition, the Marangoni stress is suppressed above CMC in a surfactant-laden surface due to surface coverage saturation [19,20], while the dilatational elastic stress exists as long as there is surface deformation in a protein-adsorbed surface due to the storage modulus of large BSA molecules [see Eq. (5)]. Therefore, our Letter exemplifies and highlights the fundamental difference between surfactant-laden and protein-adsorbed surfaces leading to distinct bubble bursting dynamics.

Notably, for bubble bursting at a Newtonian surface, bubble entrapment with the singular jetting is reported, which is caused by the finite-time singularity of the cavity collapse occurring at $Oh \approx 0.03$ of the bulk liquid [38,52]. However, our finding of bubble entrainment without jetting at a much wider Oh range of 0.003–0.02 for bubble bursting at a viscoelastic surface (Supplemental Material [29] Sec. S11) results from a distinct mechanism introduced by surface elastic stress, which is fundamentally different from previous experimental and numerical observations. The experimental results and theoretical framework may provide valuable benchmarks for future numerical investigation into bubble bursting flows with a viscoelastic surface regarding more detailed flow characterization.

In summary, we document a new bubble bursting regime, where a daughter bubble is entrapped and the jet drop ejection is suppressed with the presence of a protein-adsorbed viscoelastic surface layer, distinct from the drop ejection regime at a Newtonian surface. We reveal that the bubble entrainment is triggered by the dilatational elastic stress from surface viscoelasticity, which is essentially different from the Marangoni stress considered in surfactant systems. In practice, the entrapped small protein-enriched bubbles may enhance the gas adsorption and protein transport in liquids, and the vanishing jet drops inhibit the bubble bursting aerosolization. Thus, our finding may advance the understanding on the mass transfer related to bubble bursting in natural water bodies, bioengineering, and the food industry, where organic macromolecules are widely present forming viscoelastic surfaces. By considering the paradigmatic example of bubble bursting, we demonstrate that complex surface rheology introduces distinct and rich dynamics in multiphase, free surface flow systems.

We acknowledge Omar K. Matar, Jesse T. Ault, Chao Sun, and Vatsal Sanjay for valuable discussions and comments.

*bingqiji@cityu.edu.hk

†jiefeng@illinois.edu

‡Present address: Department of Mechanical Engineering, City University of Hong Kong, Hong Kong 999077, China.

- [1] L. Deike, Mass transfer at the ocean–atmosphere interface: The role of wave breaking, droplets, and bubbles, *Annu. Rev. Fluid Mech.* **54**, 191 (2022).
- [2] B. Ji, L. Hong, J.-T. Kim, L. P. Chamorro, and J. Feng, Dynamics of an oil-coated bubble rising in a quiescent water medium, *Phys. Rev. Fluids* **7**, 033603 (2022).
- [3] H. Lhuissier and E. Villermaux, Bursting bubble aerosols, *J. Fluid Mech.* **696**, 5 (2012).
- [4] A. M. Gañán-Calvo, Revision of Bubble Bursting: Universal Scaling Laws of Top Jet Drop Size and Speed, *Phys. Rev. Lett.* **119**, 204502 (2017).
- [5] F. Veron, Ocean spray, *Annu. Rev. Fluid Mech.* **47**, 507 (2015).
- [6] X. Wang, G. B. Deane, K. A. Moore, O. S. Ryder, M. D. Stokes, C. M. Beall, D. B. Collins, M. V. Santander, S. M. Burrows, C. M. Sultana *et al.*, The role of jet and film drops in controlling the mixing state of submicron sea spray aerosol particles, *Proc. Natl. Acad. Sci. U.S.A.* **114**, 6978 (2017).
- [7] S. D. Brooks and D. C. Thornton, Marine aerosols and clouds, *Annu. Rev. Mar. Sci.* **10**, 289 (2018).
- [8] K. Sampath, N. Afshar-Mohajer, L. D. Chandrala, W.-S. Heo, J. Gilbert, D. Austin, K. Koehler, and J. Katz, Aerosolization of crude oil-dispersant slicks due to bubble bursting, *J. Geophys. Res. Atmos.* **124**, 5555 (2019).
- [9] B. Ji, A. Singh, and J. Feng, Water-to-air transfer of nano/microsized particulates: Enrichment effect in bubble bursting jet drops, *Nano Lett.* **22**, 5626 (2022).
- [10] L. Dubitsky, O. McRae, and J. C. Bird, Enrichment of Scavenged Particles in Jet Drops Determined by Bubble Size and Particle Position, *Phys. Rev. Lett.* **130**, 054001 (2023).
- [11] L. Bourouiba, The fluid dynamics of disease transmission, *Annu. Rev. Fluid Mech.* **53**, 473 (2021).
- [12] M. Masry, S. Rossignol, B. T. Roussel, D. Bourgoigne, P.-O. Bussi ere, B. R’mili, and P. Wong-Wah-Chung, Experimental evidence of plastic particles transfer at the water-air interface through bubble bursting, *Environ. Pollut.* **280**, 116949 (2021).
- [13] R. S. Cherry and C. T. Hulle, Cell death in the thin films of bursting bubbles, *Biotechnol. Prog.* **8**, 11 (1992).
- [14] R. F. Hariadi, E. Winfree, and B. Yurke, Determining hydrodynamic forces in bursting bubbles using DNA nanotube mechanics, *Proc. Natl. Acad. Sci. U.S.A.* **112**, E6086 (2015).
- [15] T. Gutierrez, D. Berry, A. Teske, and M. D. Aitken, Enrichment of Fusobacteria in sea surface oil slicks from the Deepwater Horizon oil spill, *Microorganisms* **4**, 24 (2016).
- [16] E. T. Papoutsakis, Fluid-mechanical damage of animal cells in bioreactors, *Trends Biotechnol.* **9**, 427 (1991).
- [17] B. Ji, Z. Yang, and J. Feng, Compound jetting from bubble bursting at an air-oil-water interface, *Nat. Commun.* **12**, 6305 (2021).
- [18] Z. Yang, B. Ji, J. T. Ault, and J. Feng, Enhanced singular jet formation in oil-coated bubble bursting, *Nat. Phys.* **19**, 884 (2023).
- [19] C. R. Constante-Amores, L. Kahouadji, A. Batchvarov, S. Shin, J. Chergui, D. Juric, and O. K. Matar, Dynamics of a surfactant-laden bubble bursting through an interface, *J. Fluid Mech.* **911**, A57 (2021).

- [20] J. Pierre, M. Poujol, and T. Séon, Influence of surfactant concentration on drop production by bubble bursting, *Phys. Rev. Fluids* **7**, 073602 (2022).
- [21] J. M. Boulton-Stone, The effect of surfactant on bursting gas bubbles, *J. Fluid Mech.* **302**, 231 (1995).
- [22] K. Boniewicz-Szmyt and S. J. Pogorzelski, Evolution of natural sea surface films: A new quantification formalism based on multidimensional space vector, *Environ. Sci. Pollut. Res.* **25**, 4826 (2018).
- [23] D. Tamaro, V. Chandran Suja, A. Kannan, L. D. Gala, E. Di Maio, G. G. Fuller, and P. L. Maffettone, Flowering in bursting bubbles with viscoelastic interfaces, *Proc. Natl. Acad. Sci. U.S.A.* **118**, e2105058118 (2021).
- [24] V. Sharma, A. Jaishankar, Y.-C. Wang, and G. H. McKinley, Rheology of globular proteins: Apparent yield stress, high shear rate viscosity and interfacial viscoelasticity of bovine serum albumin solutions, *Soft Matter* **7**, 5150 (2011).
- [25] M. Campana, S. Hosking, J. Petkov, I. Tucker, J. Webster, A. Zorbakhsh, and J. Lu, Adsorption of bovine serum albumin (BSA) at the oil/water interface: A neutron reflection study, *Langmuir* **31**, 5614 (2015).
- [26] G. L. Lin, J. A. Pathak, D. H. Kim, M. Carlson, V. Riguro, Y. J. Kim, J. S. Buff, and G. G. Fuller, Interfacial dilatational deformation accelerates particle formation in monoclonal antibody solutions, *Soft Matter* **12**, 3293 (2016).
- [27] B. Noskov, A. Mikhailovskaya, S.-Y. Lin, G. Loglio, and R. Miller, Bovine serum albumin unfolding at the air/water interface as studied by dilatational surface rheology, *Langmuir* **26**, 17225 (2010).
- [28] D. Grigoriev, S. Derkach, J. Krägel, and R. Miller, Relationship between structure and rheological properties of mixed BSA/Tween 80 adsorption layers at the air/water interface, *Food Hydrocolloids* **21**, 823 (2007).
- [29] See Supplemental Material at <http://link.aps.org/supplemental/10.1103/PhysRevLett.131.104002> for materials and experimental methods, experimental observations on bubble bursting at surfaces of different solutions and wave damping during cavity collapse, theoretical comparison between the contributions of dilatational and shear elasticities at a small θ , theoretical derivation of $\nabla^s \cdot \mathbf{u} = -\ln(\Gamma/\Gamma_0)$, physical parameters and their values used in this Letter, and experimental videos, which includes Refs. [30–35].
- [30] E. Huang, A. Skoufis, T. Denning, J. Qi, R. R. Dagastine, R. F. Tabor, and J. D. Berry, OPENDROP: Open-source software for pendant drop tensiometry & contact angle measurements, *J. Open Source Software* **6**, 2604 (2021).
- [31] A. Kannan, I. C. Shieh, D. L. Leiske, and G. G. Fuller, Monoclonal antibody interfaces: Dilatation mechanics and bubble coalescence, *Langmuir* **34**, 630 (2018).
- [32] V. Sanjay, D. Lohse, and M. Jalaal, Bursting bubble in a viscoplastic medium, *J. Fluid Mech.* **922**, A2 (2021).
- [33] A. J. Mendoza, E. Guzmán, F. Martínez-Pedrero, H. Ritacco, R. G. Rubio, F. Ortega, V. M. Starov, and R. Miller, Particle laden fluid interfaces: Dynamics and interfacial rheology, *Adv. Colloid Interface Sci.* **206**, 303 (2014).
- [34] G. Narsimhan, Characterization of interfacial rheology of protein-stabilized air–liquid interfaces, *Food Eng. Rev.* **8**, 367 (2016).
- [35] D. Chandrasekharaiah and L. Debnath, *Continuum Mechanics* (Academic Press, San Diego, 1994).
- [36] C. Ybert and J.-M. Di Meglio, Ascending air bubbles in solutions of surface-active molecules: Influence of desorption kinetics, *Eur. Phys. J. E* **3**, 143 (2000).
- [37] L. G. Cascão Pereira, O. Theodoly, H. W. Blanch, and C. J. Radke, Dilatational rheology of BSA conformers at the air/water interface, *Langmuir* **19**, 2349 (2003).
- [38] F. J. Blanco-Rodríguez and J. Gordillo, On the sea spray aerosol originated from bubble bursting jets, *J. Fluid Mech.* **886**, R2 (2020).
- [39] R. H. Ewoldt and C. Saengow, Designing complex fluids, *Annu. Rev. Fluid Mech.* **54**, 413 (2022).
- [40] P. L. L. Walls, L. Henaux, and J. C. Bird, Jet drops from bursting bubbles: How gravity and viscosity couple to inhibit droplet production, *Phys. Rev. E* **92**, 021002(R) (2015).
- [41] A. K. Gaigalas, J. B. Hubbard, M. McCurley, and S. Woo, Diffusion of bovine serum albumin in aqueous solutions, *J. Phys. Chem.* **96**, 2355 (1992).
- [42] P. T. McGough and O. A. Basaran, Repeated Formation of Fluid Threads in Breakup of a Surfactant-Covered Jet, *Phys. Rev. Lett.* **96**, 054502 (2006).
- [43] X. Zhong and A. M. Ardekani, A model for bubble dynamics in a protein solution, *J. Fluid Mech.* **935**, A27 (2022).
- [44] D. A. Edwards, H. Brenner, and D. T. Wasan, *Interfacial Transport Processes and Rheology* (Butterworth-Heinemann, New York, 1993).
- [45] V. Fainerman, E. Lucassen-Reynders, and R. Miller, Adsorption of surfactants and proteins at fluid interfaces, *Colloids Surf. A* **143**, 141 (1998).
- [46] A. Jaishankar, V. Sharma, and G. H. McKinley, Interfacial viscoelasticity, yielding and creep ringing of globular protein–surfactant mixtures, *Soft Matter* **7**, 7623 (2011).
- [47] N. Jaensson and J. Vermant, Tensiometry and rheology of complex interfaces, *Curr. Opin. Colloid Interface Sci.* **37**, 136 (2018).
- [48] H. Zhang, G. Xu, T. Liu, L. Xu, and Y. Zhou, Foam and interfacial properties of Tween 20–bovine serum albumin systems, *Colloids Surf. A* **416**, 23 (2013).
- [49] V. C. Suja, M. Rodríguez-Hakim, J. Tajuelo, and G. G. Fuller, Single bubble and drop techniques for characterizing foams and emulsions, *Adv. Colloid Interface Sci.* **286**, 102295 (2020).
- [50] F. J. Blanco-Rodríguez and J. Gordillo, On the jets produced by drops impacting a deep liquid pool and by bursting bubbles, *J. Fluid Mech.* **916**, A37 (2021).
- [51] J. Lucassen, Longitudinal capillary waves. Part I.—theory, *Trans. Faraday Soc.* **64**, 2221 (1968).
- [52] L. Duchemin, S. Popinet, C. Josserand, and S. Zaleski, Jet formation in bubbles bursting at a free surface, *Phys. Fluids* **14**, 3000 (2002).